
Modelling resistance welding of thermoplastic composites with a nanocomposite heating element

Journal Title
XX(X):2–??
©The Author(s) 0000
Reprints and permission:
sagepub.co.uk/journalsPermissions.nav
DOI: 10.1177/ToBeAssigned
www.sagepub.com/



David Brassard^{1,2}, Martine Dubé^{2,3} and Jason R. Tavares^{1,2}

Abstract

Electrically conductive nanocomposite heating elements are being developed as a complement to traditional carbon fibre or stainless steel heating elements in resistance welding of thermoplastic composites. Here we present the development of a finite element model of the resistance welding process with these new heating elements, from which we establish a process window for high quality welded joints. The finite element model results were validated experimentally and a lap shear strength improvement of 28% is reported relative to previously published results. Fractography analysis of the broken joints revealed a thin-layer cohesive failure mode due to the brittleness of the nanocomposite heating elements.

Keywords

Resistance welding, Thermoplastic composite, Finite element analysis (FEA), Joints/joining, Nanocomposite

Introduction

The use of thermoplastic composite (TPC) materials is rising¹ and these materials now find applications in wind turbine and aerospace industries². Their short processing cycle, improved impact resistance, end-of-life recyclability and chemical stability³ make them good candidates for lightweight structural components compared to traditional thermoset resins. A major difference between thermosets and thermoplastics is the methods to join parts together: while adhesive bonding and mechanical assembly is the norm for thermoset composites, assemblies of TPCs are preferably produced by welding together individual components due to their ability to be melted and re-formed. Welding and adhesive bonding offer improved transfer of loads between composite components and reduced damage caused by localized stress around the mechanical fasteners⁴. Machining holes for the mechanical fasteners also induces damages to the reinforcing fibres and thus have adverse effects on the performances of composite parts. Finally, mechanical fasteners can be subject to galvanic corrosion when in contact with carbon fibres. Welding of TPCs is generally achieved by localized heating of the weld zone through resistance, induction or ultrasonic welding. It can also be achieved through alternative means such as bulk heating of the components in a press or an autoclave, or local heating with infrared heaters, lasers, hot gases or heating plates⁵. During resistance welding, the weld zone temperature increases via Joule heating of a resistive heating element (HE) located between the adherents^{5–10} (Fig. 1). This process offers good mechanical performance and short processing times of the order of minutes, and can be achieved with HE such as carbon fibre plies¹⁰, stainless steel (SS) meshes^{6–8} or, more recently, an electrically conductive nanocomposite polymer⁹.

The failure modes and lap shear strength (LSS) are frequently reported to assess the performance of welded joints. The failure modes during lap shear tests are dependent on the nature of the adherents, fibre orientations and processing conditions¹². Under optimal welding conditions, with SS meshes, light-fiber-tear failures (LFT) is often accompanied by mesh tearing due to poor adhesion between the SS heating elements

¹Department of Chemical Engineering, Polytechnique Montréal, P.O. Box 6079 Station Centre-Ville, Montréal, QC, H3C 3A7, Canada

²Research Center for High Performance Polymer and Composite Systems (CREPEC), Polytechnique Montréal, P.O. Box 6079 Station Centre-Ville

³Department of Mechanical Engineering, École de technologie supérieure, 1100 Notre-Dame Street West, Montréal, Québec, Canada, H3C 1K3

Corresponding author:

Jason R. Tavares, Department of Chemical Engineering, Polytechnique Montréal, P.O. Box 6079 Station Centre-Ville, Montréal, QC, H3C 3A7, Canada
Email: jason.tavares@polymtl.ca

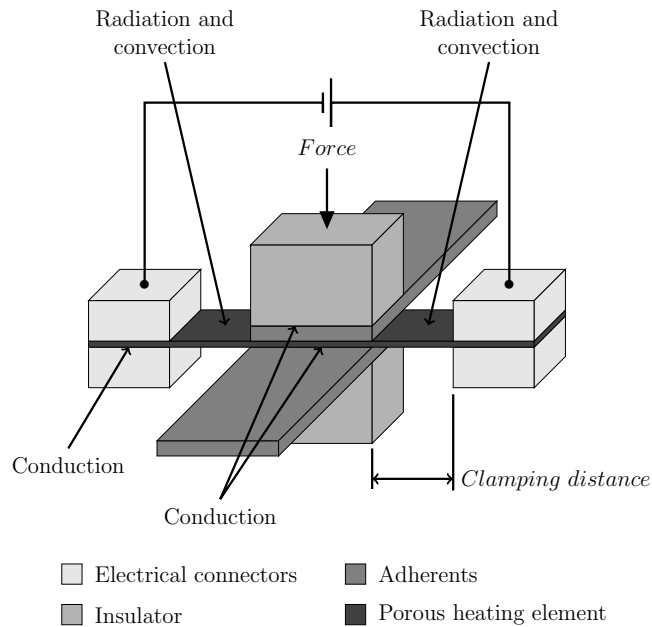


Figure 1. Schematic view of the resistance welding process highlighting local thermal transport mechanisms¹¹

and the polymer matrix^{8,13–15}. Lack of adhesion with the polymer matrix can be a limiting factor for high performance materials. Manufacturers from the space industry are looking for low density alternative heating elements that would also be resistant to corrosion.

It was recently shown that an electrically conductive nanocomposite polymer HE, composed of polyetherimide (PEI) and multi-wall carbon nanotubes (MWCNTs), can successfully weld unidirectional (UD) carbon fibre reinforced PEEK (CF/PEEK) composite adherents⁹. While this proof-of-concept illustrated how the new HE could complement SS meshes and carbon fibre HE, the effects of the welding parameters on the weld quality were not thoroughly explored. The development of a processing window is needed to assess the full capabilities of the nanocomposite HE.

The main parameters controlling the resistance welding process are the power density (electrical power divided by the heating element area), duration, welding pressure, geometry of the components of the jig holding the adherents and the properties of the materials used as thermal insulators. Good control of the heating parameters is required to keep the heat-affected zone (HAZ) as close as possible to the bonding surfaces to avoid deconsolidation and fibre movements⁶. The power density

and process duration affect the size and shape of the HAZ by controlling the rate and amount of energy dissipated within the weld, while pressure on the laminates prevents the formation of porosity from deconsolidation of the plies¹⁶. For a given welding jig configuration, the clamping distance (CD) and the dimensions and nature of the electrodes dictate edge effects, which are caused by the sharp transition in the heat dissipation mechanism of the HE from conduction in the weld and adherents to radiation and potentially convection outside the weld as illustrated in Fig. 1¹⁷. Edge effects can have a strong impact on the temperature distribution within the weld. Inappropriate adjustment of the CD may lead to incomplete welding or degradation at the edges¹⁸. Finally, the thermal properties and geometry of the insulators will have a strong impact on optimal processing parameters, making those parameters dependant on the design of the welding jig^{17–20}. Going from an experimental jig to a production setup requires careful considerations and a deep understanding of the welding process.

A process window that compounds all these effects cannot be obtained solely through physical experiments, because key processing information is unavailable. Namely, the inability to install thermocouples within the weld without disturbing the process limits the ability to measure the temperature at the interface when using a nanocomposite HE. The air gap between the adherent and the nanocomposite, induced by the introduction of a thermocouple within the weld, instead of a flat contact of both surfaces (when no thermocouple is present), changes the transport mechanism of the heat generated by the heating element from conduction between the components to poor conduction through air. The presence of a thermocouple in the weld directly leads to rapid overheating and thermal degradation of the heating element, while only a fraction of the heat is transferred to the adherent. On the other hand, with the same welding parameters, a weld can be produced with minimal thermal degradation when the thermocouple is not present. However, information gained through preliminary experiments with thermocouples located outside the weld can be used to help develop a finite element model of resistance welding with a nanocomposite HE, which will in turn guide subsequent exploration of the welding parameters.

Modelling resistance welding of composites with finite element models is not a new concept. It has been extensively used to investigate welding parameters^{17,21,22} with the goal of optimizing welding conditions¹⁹. It was also recently used to extend resistance welding from single welds to continuous welding conditions²⁰. In all those case, finite element models were successfully developed to guide or extend experimental studies.

Therefore, this article presents the development and validation of a transient finite element model for resistance welding of thermoplastic composites with a nanocomposite HE. This model is subsequently used to predict good welding

conditions and establish a processing window leading to improved mechanical performances. The model evaluates the effects of welding parameters on the temperature distribution and profile in the joint over time with the goal of establishing a processing window leading to good weld quality and mechanical performance based on these results.

Methodology

Resistance welding finite element model

A 3D transient finite element model of the resistance welding process is developed with the COMSOL Multiphysics® software. This model evaluates the electrical field in the electrodes and nanocomposite HE, Joule heating of the nanocomposite HE, heat transfer in the solids, heat dissipation through convection and radiation and thermal contact conductance between critical components. The geometry of the components is detailed in Fig. 2. The gaps identified in the geometry were 0.1 mm. The finite element model is composed of 3D tetrahedral elements with local mesh refining in the heating element, the adherents and the surrounding volumes. The mesh is recomputed for each value of CD as it has a direct impact on the geometry of the model. A convergence analysis confirmed that meshes with approximately 70 000 to 90 000 elements provides results similar to finer meshes, but with reduced computational time. This produced systems of equations with 150 000 to 200 000 degrees of freedom. The model was configured with a direct PARADISO solver instead of the default iterative solver.

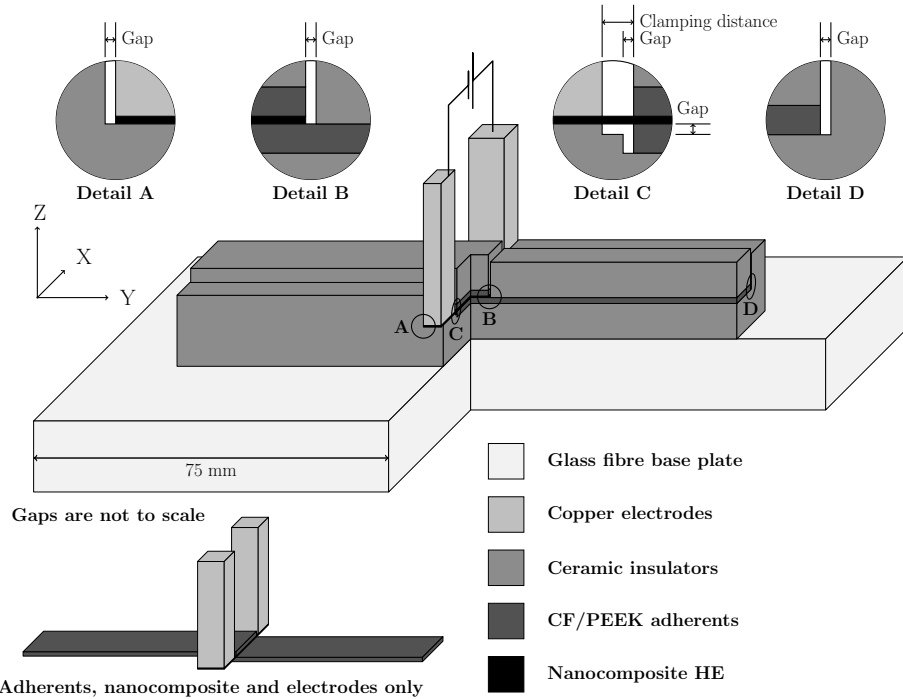


Figure 2. Three-quarter section view of the geometry of the model highlighting the components of the model and location of the 0.1 mm air gaps¹¹

Electrical field evaluation The model evaluates the electrical field in the nanocomposite HE and the electrodes. The resulting field is used to compute the Joule losses from current and electrical resistance. The constitutive rules for conservation of current and charges are imposed, with the application of the general equations 1 to 3 describing the electrical field within the nanocomposite HE and the copper electrodes (a nomenclature of all symbols and their respective units is presented at the end of the article). The equation of continuity (Eq. 1) defines that the divergence (∇) of the current density (\mathbf{J}) is equal to the current source (Q_j) (both expressed in A m^{-2}). Ohm's law (Eq. 2) defines that the current density (\mathbf{J}) is equal to the sum of imposed external current density (\mathbf{J}_e in A m^{-2}) and the product of the sum of the electrical conductivity (σ_{ele} in S m^{-1}) and the product of the permittivity of vacuum (ϵ_0 in F m^{-1}) and the relative permittivity (ϵ_r a dimensionless value) as function of time with the electric field (\mathbf{E} in V m^{-1}). Finally, Eq. 3 defines the electric field (\mathbf{E} in V m^{-1}) as the negative of divergence (∇) of the electric potential (V in V).

$$\nabla \cdot \mathbf{J} = Q_j \quad (1)$$

$$\mathbf{J} = \left(\sigma_{ele} + \varepsilon_0 \varepsilon_r \frac{\partial}{\partial t} \right) \mathbf{E} + \mathbf{J}_e \quad (2)$$

$$\mathbf{E} = -\nabla V \quad (3)$$

As in the laboratory experiment, a constant power input was applied to the top surface of an electrode as boundary condition. The top surface of the second electrode was set as a ground connection with an electrical tension of 0 V. The other outer edges of the nanocomposite and electrodes were considered as electrical insulators and their boundary conditions were defined as per equation 4 which defines that the current density perpendicular to the boundary is equal to 0.

$$\mathbf{n} \cdot \mathbf{J} = 0 \quad (4)$$

Heat transfer within solids An energy balance (Eq. 5) with Fourier's law of heat conduction is calculated for all constituents of the model.

$$Q_e = \rho C_p \frac{\partial T}{\partial t} + \nabla \cdot -k \nabla T \quad (5)$$

The one-way coupling between the thermal and electrical components of the model is obtained through an electromagnetic heat source from resistive losses (Q_e). That heat source is defined (Eq. 6) as the product of the current density (\mathbf{J} in A m^{-2}) and the electric field (\mathbf{E} in V m^{-1}).

$$Q_e = \mathbf{J} \cdot \mathbf{E} \quad (6)$$

The boundary layer thickness was evaluated with the Boussinesq approximation to confirm on which surfaces convective cooling boundary conditions should be considered. For $Pr > 0.6$, the thickness can be evaluated with Eq. 7 with the Grashof number for a specific length (Gr_L) defined as in Eq. 8²³. To confirm the validity of this equation, the Prandtl number (Pr) was evaluated with Eq. 9. Based on the properties of air, the boundary layer thickness was evaluated to be at least 5 mm thick for a specific length of 12.7 mm that is representative of the height of the section enclosed between the sides of the welded joint and the electrodes.

$$\delta = 5L \left(\frac{Gr_L}{4} \right)^{-1/4} \quad (7)$$

$$Gr_L = \frac{g\beta (T_s - T_\infty) L^3}{\nu^2} \quad (8)$$

$$Pr = \frac{C_p \mu}{k} \quad (9)$$

Considering that the CD (Fig. 2) is usually less than 2 mm, it is assumed that no convective cooling takes place in the gaps of the model and in the enclosed space between the sides of the composite and the electrodes. The thickness of the boundary layer required to obtain natural convective cooling was calculated to be approximately 5 mm under the current conditions, using the Boussinesq approximation. For the other outer surfaces of the model, natural convection described as in Eq. 10 is applied. The natural convection coefficient (h_{conv}) for vertical surfaces with $10^4 < Pr Gr < 10^9$ can be approximated with Eq. 11 at $20 \text{ W m}^{-1} \text{ K}^{-1}$. This value is applied as a constant in the model for all outer surfaces.

$$-\mathbf{n} \cdot \mathbf{q} = -h_{conv} (T_s - T_\infty) \quad (10)$$

$$h = \frac{0.59 \lambda_{air} (Pr Gr_L)^{0.25}}{L_c} \quad (11)$$

The surface temperature of the exposed sections of the nanocomposite is high enough that radiative cooling must be accounted for, as defined in Eq. 12. An emissivity of 1 was defined in the model as a first approximation.

$$-\mathbf{n} \cdot \mathbf{q} = \varepsilon \sigma_{SB} (T_\infty^4 - T_s^4) \quad (12)$$

The surfaces within the gaps of the model are considered to be thermally isolated to simulate imperfect contact between the insulator blocks.

Thermal contact conductance Imperfect thermal contact between components is simulated with a thermal contact resistance that is inserted between the composite adherents and the ceramic insulators in the sections directly above and under the welded zone. The Cooper-Mikic-Yovanovich correlation²⁴ (Eq. 13 to 17) which is based on the surfaces roughness, the contact pressure and physical properties defines a thermal contact conductance coefficient (h_c). For the conductance of the interstitial gas (h_g), a value of $0.0262 \text{ W m}^{-2} \text{ K}^{-1}$ was used to simulate air²⁵. The total conductance coefficient (h) is then applied in the model as shown in Eq. 18 and 19.

$$h = h_c + h_g \quad (13)$$

$$h_c = 1.25 \times k_{contact} \frac{m_{asp}}{\sigma_{asp}} \left(\frac{p}{H_c} \right)^{0.95} \quad (14)$$

$$\frac{1}{k_{contact}} = \frac{1}{2} \left(\frac{1}{k_1} + \frac{1}{k_2} \right) \quad (15)$$

$$\sigma_{asp} = \sqrt{\sigma_{asp,1}^2 + \sigma_{asp,2}^2} \quad (16)$$

$$m_{asp} = \sqrt{m_1^2 + m_2^2} \quad (17)$$

$$-\mathbf{n}_1 \cdot (-k_1 \nabla T_1) = -h (T_2 - T_1) \quad (18)$$

$$-\mathbf{n}_2 \cdot (-k_2 \nabla T_2) = -h (T_1 - T_2) \quad (19)$$

Material

The matrix of the nanocomposite HE is composed of PEI (CAS 61128-46-9) pellets ordered from Sigma Aldrich. It has a melt index of 18 g per 10 min at 337 °C with a mass of 6.6 kg and its molecular weight is M_n of 15.0 kg mol⁻¹ and M_w of 21.6 kg mol⁻¹. To obtain a conductive nanocomposite, dry powdered MWCNTs, produced by combustion chemical vapour deposition (CCVD), purchased from Raymor Industries, were added to the PEI. They had outer diameters of 10 to 20 nm, lengths ranging from 1 to 12 μm and purity of at least 99%.

The PEI pellets and 10% weight fraction of MWCNTs were fed and mixed together in a twin-screw extruder at 340 °C. The filament was cut into pellets, mixed and compounded two more times to obtain a uniform batch. Flat nanocomposite heating elements were then produced by hot-pressing and consolidating, at 340 °C, the resulting PEI/MWCNT pellets to a film with a nominal thickness of 0.65 ± 0.1 mm. 12.7 mm wide and 55 mm long HE were cut from this film. Although percolation can be achieved with much lower MWCNT content, a 10% weight fraction was required to reach a conductivity close to our target of 1 S cm⁻¹. This high conductivity was necessary to limit the voltage during the welding process and thus reduce current leakage within the composite adherents.

The TPC adherents were produced by compression moulding 16 plies of pre-impregnated CF/PEEK to form unidirectional (UD) laminates. The plies were heated to 390 °C under a pressure of 0.25 MPa, in agreement with the supplier's recommendations. The pressure was then increased to 1 MPa for 30 minutes and the laminates were finally cooled down to room temperature over approximately 60 minutes while maintaining the pressure. The laminates were then cut to dimensions (25.4 x 101.6 mm), according to ASTM D5868 - 01(2014), with a water jet cutting machine. The adherents were 2.1 mm thick.

12.7 mm thick soft unfired alumina silicate ceramic sheets served as thermal insulators. Blocks were cut with an abrasive saw and sanded to final dimensions. The ceramic insulator blocks are installed on a 25 mm thick 300 mm by 600 mm GPO3 glass fibre composite plate. The electrodes were machined from a 12.7 mm thick sheet of UNS C14500 phosphorous tellurium copper.

Material characterization

The properties of the copper electrodes were taken from COMSOL's database and the properties of the GPO3 glass fibre plate were taken from the supplier's information. For critical components, material properties were measured whenever possible. Tables summarizing all the material properties are presented in the Supplementary Information document.

Thermal and physical properties The thermal conductivity of the nanocomposite, the TPC adherents (parallel and perpendicular to the fibres) and the ceramic insulators were measured at 20 °C intervals between 40 °C and 200 °C with the modified transient plane source (MTPS) method (ASTM D7984 - 16) using a C-Therm TCi Thermal Conductivity Analyzer in an environmental chamber. The method works by applying a constant current heat source to one side of a sample (raising its temperature by 1 to 3 °C). Some heat is absorbed by the sample, whereas the rest causes a temperature rise at the sensor surface: the higher the thermal conductivity of the sample, the more heat is absorbed and the lower the temperature rise at the sensor surface. This allows for the direct measurement of thermal conductivity (k) and thermal effusivity ($\sqrt{\rho C_p k}$). Simplified series of linear approximation fitted over the measured thermal conductivity values were used in the model instead of the raw data to smooth out the signal. Constant values of 0.27 and 400 W m⁻¹ K⁻¹ were used respectively for GPO3 and copper.

The specific heat (C_p) of the nanocomposite HE, the TPC adherents and the alumina silicate insulators were measured by modulated differential scanning calorimetry (MDSC) (ASTM E2716 - 09(2014) method B) with a TA Instruments Q2000. Tests

were conducted under isothermal conditions with an amplitude of $\pm 1^\circ\text{C}$ and a period of 100 s on 15 mg samples. Measurements were obtained at 40 °C, at 10 °C below and above the glass transition and melting temperatures (when applicable) and at 400 °C. To account for the enthalpy of melting, an additional point was added for the TPC adherents at 343 °C (T_m). For the alumina silicate, a single measurement was taken at 97 °C. For the GPO3 and copper, constant values of 1260 and 385 J kg⁻¹ K⁻¹ were used, respectively. The properties for copper were taken from COMSOL's library of materials and the properties for GPO3 were taken from manufacturer specifications.

The density as a function of temperature of the CF/PEEK adherents was taken from the literature¹⁸ while the density at room temperature for the nanocomposite was measured (ASTM D792 – 13) to be 1320 kg m⁻³. The density of the alumina silicate ceramic was measured to be 2500 kg m⁻³ and a density of 1800 kg m⁻³ was taken from the supplier's information for GPO3. COMSOL's reported density of 8700 kg m⁻³ was used for the copper electrodes.

Electrical properties The electrical conductivity of the nanocomposite was previously measured by the four-point method to be 0.8 S cm⁻¹⁹. Its relative permittivity is estimated with the law of mixtures to be 4.3 based on the relative permittivity published in SABIC's documentation for ULTEM 1010 PEI and the reported value for MWCNTs²⁶.

Surface properties The surface profile of TPC adherents was measured with a ContourGT 3D Optical Microscope from Brueker. Roughness (σ_{asp}) and average asperities slope (m_{asp}) were extracted from the profile with the software Gwyddion.

Mechanical properties The tensile strength and elongation at break of the nanocomposite were measured from five type IV specimens according to ASTM D638-14 with an Instron 3365 Universal Testing Systems and a 5 kN load cell. The LSS of each weld was evaluated with a crosshead speed of 13 mm min⁻¹ on an MTS Alliance RF/200 testing machine as per ASTM D5868-01(2014) with the exception that samples had a nominal overlap length of 12.7 mm instead of 24.5 mm. SEM fractography analysis was performed on some specimens with a Hitachi TM3000. The surfaces were sputter coated with a thin layer of gold and palladium.

Welding experiments

The welding experiments were conducted with a custom computer-controlled resistance welding jig. The nanocomposite HE was located between the two adherents in the welding zone with an overlap of 12.7 mm and a width of 25.4 mm. The

electrical connection to the nanocomposite HE was achieved by two square-ended copper electrodes. Alumina silicate ceramic insulator blocks surrounded the adherents. A pressure of 2.4 MPa was applied by the copper electrodes on the nanocomposite HE to minimize contact resistance and a pressure of 1.0 to 1.4 MPa was applied on top of the welding zone. The CD for each electrode was carefully adjusted with gauges. The copper electrodes were connected to a 10 kW programmable DC power supply series XR from Magna-Power capable of providing up to 160 V and 60 A. The power supply was set up to operate at a constant power output during each test. The power for each test was calculated based on the power density and the area of the nanocomposite between the electrodes, accounting for the area within the CD in addition to the area within the weld. The power density, the CD, the pressure on the weld and the time during which power is applied were varied during the experiments. Four K type thermocouples were located between the top adherent and the alumina silicate ceramic insulator block above the welding zone, as shown in Fig. 3, to serve as reference points to compare with the model. Thermocouples could not be located inside the weld as they were subject to electrical interferences, even when protected by Kapton® tape, and they altered the heat transfer mechanism leading to premature degradation.

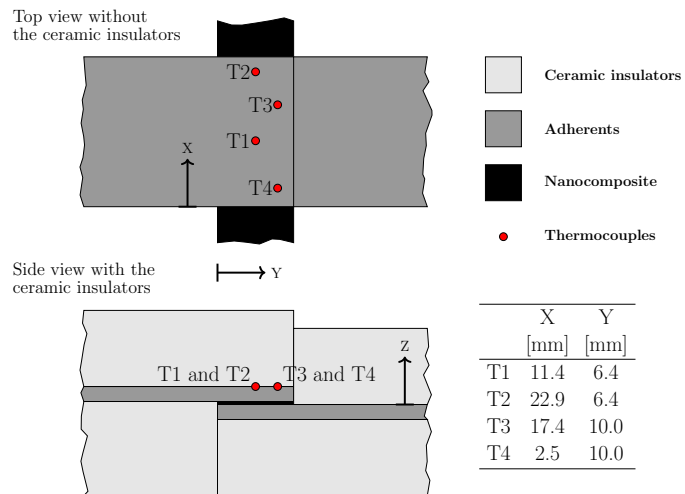


Figure 3. Location of thermocouples during welding experiments

Results and discussion

Material characterization

The C_p obtained by MDSC are presented at Table 1. The thermal conductivity as a function of temperature for CF/PEEK, the PEI/MWCNT nanocomposite and the alumina silicate are reported in Table 2. The asperities roughness σ_{asp} and asperities average slopes m_{asp} were measured respectively at $0.26\ \mu\text{m}$ and 0.15 . The microhardness was set at $0.1\ \text{GPa}$ in the model.

Temperature [°C]	CF/PEEK [J kg ⁻¹ K ⁻¹]	PEI/MWCNT [J kg ⁻¹ K ⁻¹]	Alumina Silicate [J kg ⁻¹ K ⁻¹]
40	926	1059	
97			975
139	1265		
159	1359		
207		1561	
227		1765	
310	1809		
343	2400		
360	1792		
399	1790	1955	

Table 1. Results for Specific heat measurements

Temperature [°C]	CF/PEEK Parallel [W m ⁻¹ K ⁻¹]	CF/PEEK Perpendicular [W m ⁻¹ K ⁻¹]	PEI/MWCNT [W m ⁻¹ K ⁻¹]	Alumina Silicate [W m ⁻¹ K ⁻¹]
20	2.25	0.55	0.41	
40			0.43	5.7
60			0.43	
110			0.46	
150			0.48	
200	3.02	0.73		

Table 2. Results for thermal conductivity measurement

Nanocomposite's dispersion state

The dispersion state of the MWCNTs could not be evaluated by SEM or TEM observations due to the high weight fraction of the resulting nanocomposite. Such a high weight fraction has the potential to yield a nanocomposite containing agglomerated clusters of MWCNTs. The presence of inter-connected clusters

contributes to the conductivity by providing pathways of connected nanotubes^{27,28}. On the other hand, poor dispersion of the MWCNTs, and the resulting clusters, may have detrimental effects on the bulk mechanical properties of the nanocomposite.

Modelling results

The model was first validated with experimental data. Four resistance welding experiments under different conditions served as references. The same welding conditions were reproduced by the model and the resulting validation curves are presented in Fig. 4. Initial modelling efforts neglected the electrical contact resistance between the electrodes and the nanocomposite and did not fit the observations. Upon further inspection, the contact electrical resistance was measured by subtracting the theoretical nanocomposite's HE electrical resistance to the total resistance of the welding setup between both electrodes measured with a handheld multimeter. The electrical contact resistance accounts for approximately 50% of the total electrical resistance of the setup. Reducing the power by 45% provided a good agreement with the experiments allowing for the model to explore the general behaviour of the welding process.

As it was not possible to monitor the temperature directly at the weld interface without disturbing the thermal profile and affecting the results, the model offers us insight that could not be obtained from experiments. The temperature distribution along the length of the weld (*x-axis*) varies based on the CD and power density, as previously reported¹⁸ (Fig. 5). It can be controlled with a variation of the CD but the profile across the width of the weld (*y-axis*) is mostly unaffected by the CD. A cold edge (at $y = 0$ mm in Fig. 5) is always present at the top surface of the nanocomposite on the side where the adherent exits the weld due edge effects caused by the high axial thermal conductivity of the carbon fibres in the UD TPC adherents. On the bottom surface of the nanocomposite, the cold edge is located on the mirror side of the weld (at $y = 12.7$ mm) due to the adherent leaving the weld on the other side (details in bottom sections of Fig. 2 and Fig. 3).

Simulations were performed to observe the temperature uniformity along the length of the weld (*x-axis*) to optimize the CD and to evaluate the sensitivity of this parameter. The optimal CD is the distance which minimizes the temperature difference between the centre of the weld and the maximum temperature at the edges. Polymer degradation at the edge begins when the CD is too large. The CDs for both conditions vary almost linearly as a function of the power density over the experimental domain (Fig. 6). Additionally, an almost constant difference of 0.4 mm exists between the optimal CD

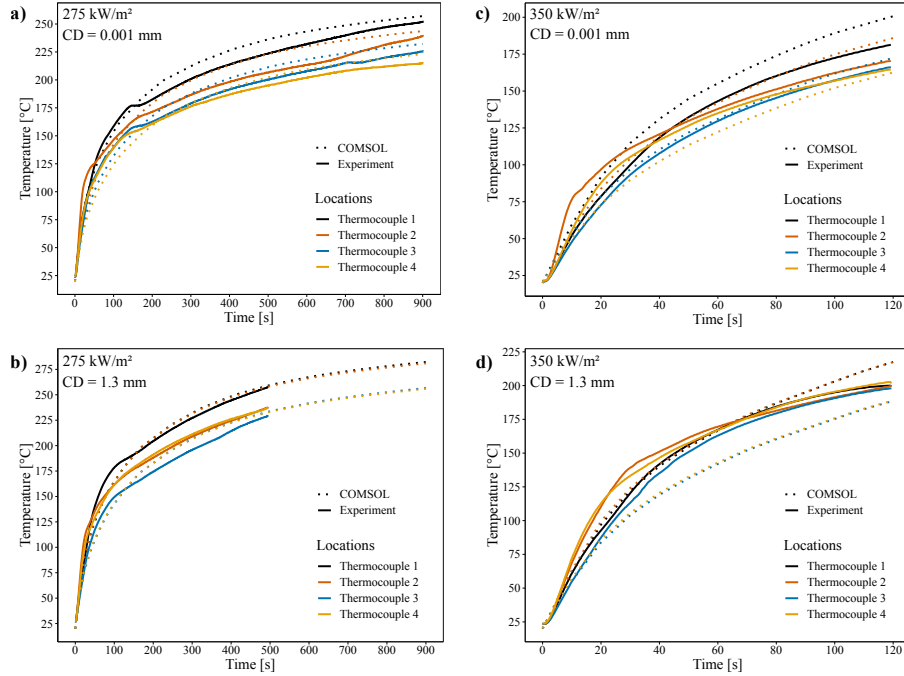


Figure 4. Validation curves for the model under various welding conditions with solid line representing experimental results, dotted lines for COMSOL results and colours assigned to each thermocouple locations¹¹

and the length causing thermal degradation at the edge. Thus, the dimensional tolerance for the location of the electrodes during the resistance welding with a nanocomposite HE process can be on the order of a few tenths of millimetres.

It is now possible to expand the scope of the analysis. The resulting process window (Fig. 7) presents the time required for the hottest point at the interface to reach 370 °C, 400 °C and 440 °C, 10 °C below the degradation temperature of PEI²⁹. The temperature of the lower bound and the average temperature within the weld at that moment (approximately 390 °C) are higher than the reported temperatures required to obtain reptation times compatible with the resistance welding process for PEI/PEEK interfaces³⁰. On the other hand, the addition of a large fraction of MWCNT is limiting polymer chain mobility at lower temperatures^{31,32} and a higher temperature or more time is required to achieve similar diffusion of the chains. Additional welding experiments were conducted based on the suggested processing window and previous results to validate the model's results. The average single lap shear strength for all welded joints are presented in Fig. 7.

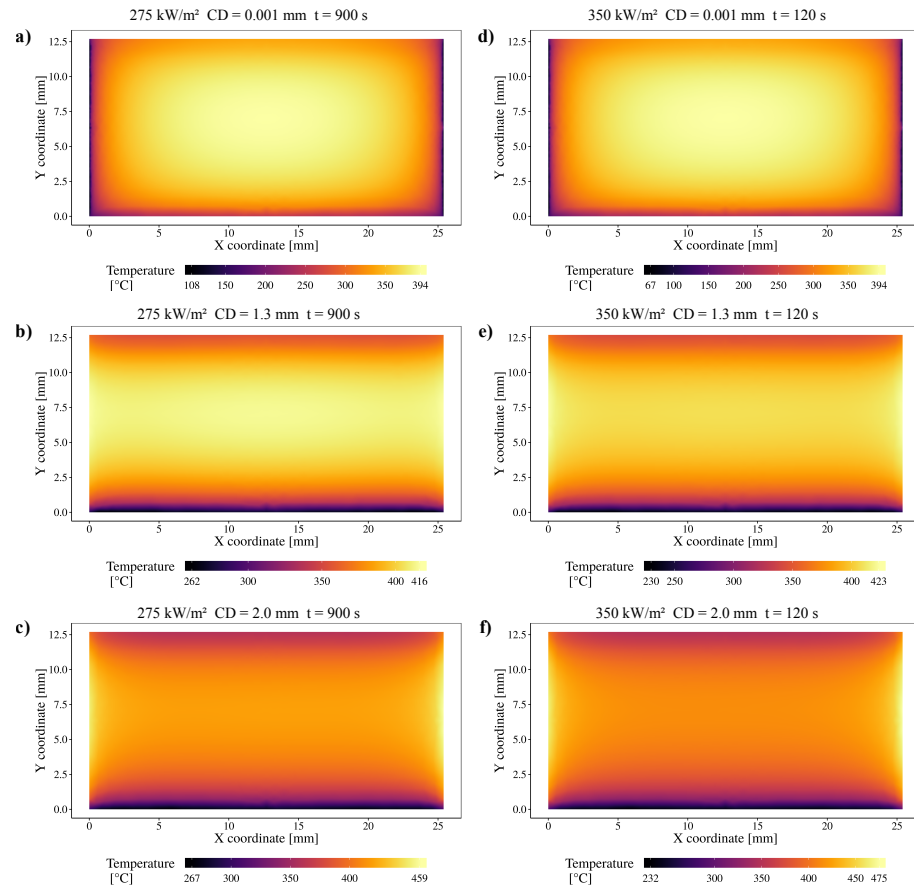


Figure 5. Temperature distributions after 900 and 120 seconds for respective power densities of 275 and 350 kW m^{-2} at the interface on top of the nanocomposite HE with CDs of 0.001 , 1.3 and 2.0 mm^{11}

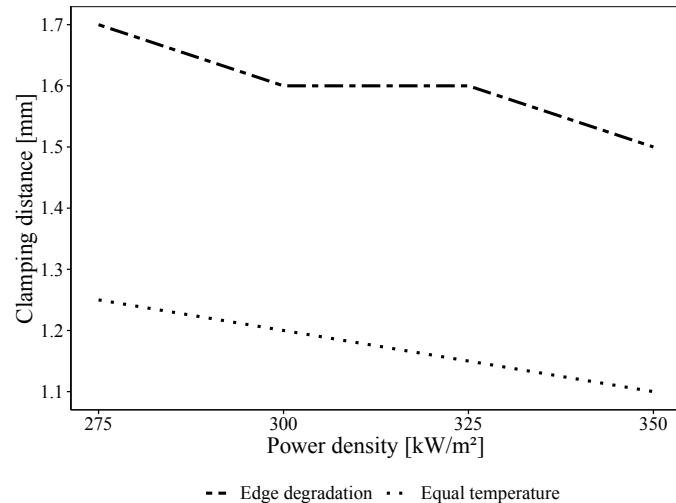


Figure 6. Sensitivity analysis for the CD showing the CDs resulting in optimal temperature distribution and the beginning of edge degradation as a function of power density¹¹

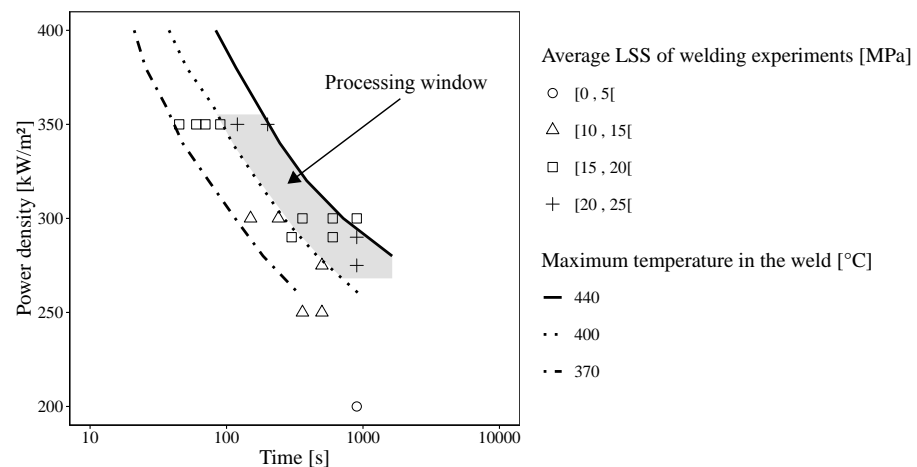


Figure 7. Process window (grayed zone) based on the simulation results with optimal CD, the lines represent the time to reach a local maximum temperatures of 370 °C, 400 °C and 440 °C on the top surface of the nanocomposite in the model while the markers presents average LSS results from all the welding experiments, no data points were recorded with average LSS between 5 and 10 MPa¹¹

Welding experiments

Current leakage in the composite adherents can be a problem for resistance welding of carbon fibre laminates at high power and it currently limits resistance welding with a nanocomposite HE to unidirectional adherents. The model pointed toward the possibility to produce welds at lower power and longer times to reduce the voltage difference along the length of the nanocomposite HE to minimize the risk of current leakage. Successful welding tests were performed with power densities as low as 250 kW m^{-2} (resulting LSS $\sim 14 \text{ MPa}$). These additional tests, along with previous results are included in Fig. 7 and in Table 3 and 4. The highest average LSS (24.9 MPa) was obtained at a power density of 350 kW m^{-2} , a CD of 1.3 mm, a pressure of 1 MPa on the weld and a welding time of 120 s. The high variance of the LSS, under these welding conditions, come from individual LSS values ranging between 14.1 and 35.2 MPa (the full data set is available in the online repository listed in reference¹¹). The average LSS corresponds to a 28% improvement relative to previously published results⁹, thanks to a better processing window predicted by the finite element model. LSS results of joints welded using non-optimal sets of welding parameters are also presented in Table 3 and 4¹¹. A welding experiment at 200 kW m^{-2} during 900 s did not result in a successful weld as the joint did not reach temperatures high enough to allow polymer chain reptation across the interface. The design for the joints in this study omitted the integration of a PEI film on the faces of the adherents. Another explanation for the high temperature required to obtain a weld is the almost non-existent diffusivity between PEI and PEEK below the melting temperature of PEEK. Further experiments should integrate a co-moulded PEI layer on the adherents to promote diffusion at low temperature.

Power density [kW m ⁻²]	Clamping distance [mm]	Pressure [MPa]	Values				Time [s]			
			45	60	70	90	120	150	200	
300	1.2	1.0	LSS ± S.D. Samples	[MPa]					14.9 ± 5.6 3	
350	0	1.0	LSS ± S.D. Samples	[MPa]				15.2 ± 1.7 4		
	1.0	1.0	LSS ± S.D. Samples	[MPa]				13.0 ± 4.4 3		
	1.1	1.0	LSS ± S.D. Samples	[MPa]	17.4 ± 3.6 3				21.0 ± 5.6 3	
	1.3	1.0	LSS ± S.D. Samples	[MPa]				24.9 ± 9.7 4		
	1.5	1.0	LSS ± S.D. Samples	[MPa]	16.4 ± 7.8 3	18.6 ± 2.0 3	15.5 ± 3.8 3	19.6 ± 3.5 3		

Table 3. LSS tests results¹¹

Power density [kW m ⁻²]	Clamping distance [mm]	Pressure [MPa]	Values				Time [s]			
			240	300	360	500	600	900		
200	0	1.0	LSS ± S.D. Samples	[MPa]					3.1 ± NA 1	
250	0	1.0	LSS ± S.D. Samples	[MPa]	13.2 ± NA 1		14.1 ± NA 1			
275	0	1.0	LSS ± S.D. Samples	[MPa]					20.0 ± 2.7 4	
	1.3	1.0	LSS ± S.D. Samples	[MPa]			24.3 ± NA 1			
290	0	1.0	LSS ± S.D. Samples	[MPa]					17.8 ± 2.2 4	
		1.4	LSS ± S.D. Samples	[MPa]					21.4 ± 2.7 2	
	1.2	1.0	LSS ± S.D. Samples	[MPa]		18.9 ± 7.0 3		17.7 ± 4.3 3		
300	0	1.0	LSS ± S.D. Samples	[MPa]	13.8 ± 3.8 3		17.7 ± 1.1 3		16.5 ± 0.7 3	
	1.2	1.0	LSS ± S.D. Samples	[MPa]				19.4 ± 3.0 3		

Table 4. LSS tests results (continued)¹¹

Nanocomposite tensile strength

Due to the high loading of MWCNTs in the nanocomposite and the possible presence of clusters, it is expected that its ductility and tensile strength are impacted. Average tensile strength of 72.2 ± 19.4 MPa and elongation at break of $5.2 \pm 1.7\%$ were obtained from tensile tests on nanocomposite samples. During these tests, all samples had brittle failure mode without a ductile plateau. This can be contrasted to virgin properties of ULTEM 1010 (tensile strength of 110 MPa and 60% elongation) to show that the mechanical behaviour of the nanocomposite is severely affected by the 10% wt. loading of MWCNTs, which was also noticeable during the handling of the HE. The variability in the performances of the nanocomposite is in line with the variability observed in the LSS tests.

Fractography

Direct imaging of the fractured surfaces (Fig. 8) provided some insight on the failure modes of the welded joints. First, signs of unstable crack propagation due to the brittleness of the nanocomposite are clearly visible. Evenly spaced cracks in the matrix residues are visible on one face (Fig. 8a) and evenly spaced ridges are visible in the mirror matching face (Fig. 8b). A close look at those ridges (Fig. 8c) shows polymer well bonded to the composite substrate. Second, broken fibres can be seen embedded on top of nanocomposite residues still attached to opposing faces (Fig. 8d). Both of these observations are signs that the bonding between the nanocomposite and the composite adherents is not the weakest link. Signs of thermal degradation could be observed in Fig. 8e serving as an example of porosities left by vaporized polymer. Carbon fibres with no polymer attached to them or degraded polymer residues can be seen at other locations. Finally, when thermal degradation and unstable cracks combine in the same zone, a different failure mode can be observed where cracks form between adjacent porosities and through the nanocomposite (Fig. 8f).

The SEM observations, reduced tensile strength and low elongation at break of the nanocomposite combine to infer that the current limiting factor for resistance welding of thermoplastic composites with a nanocomposite HE is the nature of the nanocomposite itself. In traditional resistance welding, a compliant resin rich layer is present between the adherents and can dissipate energy through plastic deformation. With the current brittle nanocomposite, as soon as cracking occurs, cracks will propagate in an unstable fashion through the interface. Improvements to the process could come either by combining the brittle nanocomposite with an underlying compliant layer of material to produce a flexible joint or by modifying

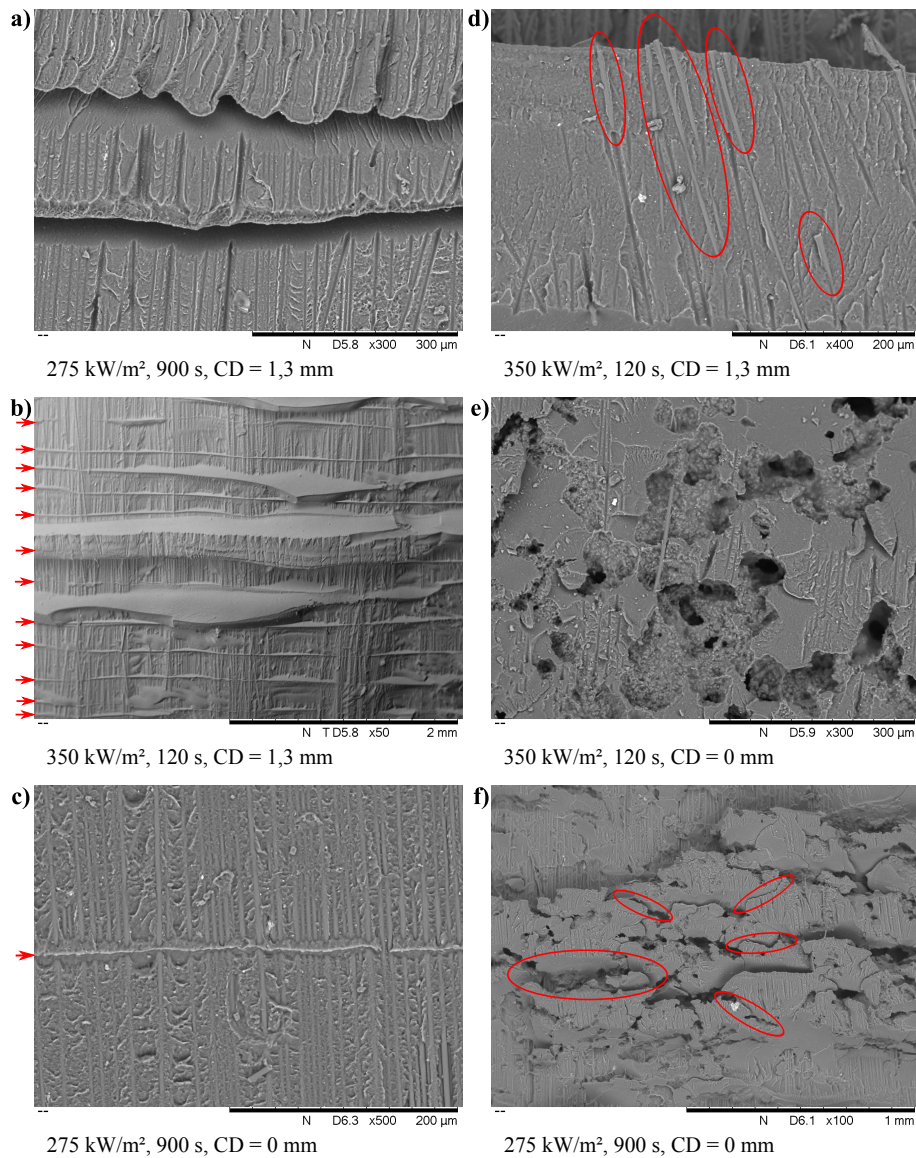


Figure 8. SEM fractography of welded specimens showing : a) unstable crack propagation causing evenly spaced cracks in the nanocomposite, b) and c) ridges left on the opposing surface when cracks forms highlighted with red arrows, d) fibre adherence to the nanocomposite HE highlighted with red ellipses, e) signs of localized thermal degradation, f) unstable crack propagation combined with thermal degradation leading to cracks identified by red ellipses between porosities¹¹.

the composition of the nanocomposite to increase its ductility while maintaining its electrical conductivity.

Conclusion

This work presented the development of a finite element model for the resistance welding of thermoplastic composites, using a nanocomposite heating element. The model allowed to establish a processing window leading to an improvement of up to 28% in the LSS of welded joints. Furthermore, the model and new experiments presented here increased our knowledge of the phenomena at play when welding using these newly developed HE. The model demonstrated the possibility to produce welds at lower power densities and this was validated experimentally. Finally, mechanical testing and fractography analysis of the nanocomposite HE highlighted its brittle nature which is currently the limiting factor in the mechanical strength of the welded joints. Future work will aim at producing a conductive nanocomposite with a higher ductility than the current solution or to bond the nanocomposite to a compliant intermediary layer.

Acknowledgements

This work was supported by ArianeGroup and CREPEC. The authors would also like to thank Vincent Rohart for his time and help for the SEM imaging and Prof. Philippe Pasquier for the thermal conductivity measurements.

Nomenclature

β	$^{\circ}\text{C}^{-1}$	Coefficient of thermal expansion of air
λ_{air}	$\text{W m}^{-2} \text{K}^{-1}$	Thermal conductivity of air
\mathbf{E}	V m^{-1}	Electric field intensity
\mathbf{J}_e	A m^{-2}	Electron current density
\mathbf{J}	A m^{-2}	Current density
\mathbf{n}_1	[]	Normal vector toward exterior of material 1
\mathbf{n}_2	[]	Normal vector toward exterior of material 2
\mathbf{n}	[]	Normal vector
\mathbf{q}	W m^{-2}	Heat flux
μ	[Pa s]	Dynamic viscosity
∇T	K m^{-1}	Temperature gradient
∇T_1	K m^{-1}	Temperature gradient in material 1

∇T_2	[K m $^{-1}$]	Temperature gradient in material 2
ν	[m 2 s $^{-1}$]	Kinematic viscosity
ρ	[kg m $^{-3}$]	Density
σ_{ele}	[S m $^{-1}$]	Electrical conductivity
$\sigma_{asp,1}$	[m]	Asperities average height (surface roughness) of material 1
$\sigma_{asp,2}$	[m]	Asperities average height (surface roughness) of material 2
σ_{asp}	[m]	Asperities average height (surface roughness)
σ_{SB}	[W m $^{-2}$ K $^{-4}$]	Stefan–Boltzmann constant
ε	[]	Surface emissivity
ε_0	[H m $^{-1}$]	Permittivity of vacuum
ε_r	[]	Relative permittivity
C_p	[J kg $^{-1}$ K $^{-1}$]	Specific heat capacity at constant pressure
g	[m s $^{-2}$]	Acceleration due to Earth's gravity
Gr_L	[]	Grashof number for vertical flat plates
h_{conv}	[W m $^{-2}$ K $^{-1}$]	Coefficient of convection
h	[W m $^{-2}$ K $^{-1}$]	Total thermal contact conductance
H_c	[Pa]	Microhardness of the softer material
h_c	[W m $^{-2}$ K $^{-1}$]	Contact conductance
h_g	[W m $^{-2}$ K $^{-1}$]	Interstitial gas conductance
h_{conv}	[W m $^{-2}$ K $^{-1}$]	Convective heat transfer coefficient
k	[W m $^{-1}$ K $^{-1}$]	Thermal conductivity
k_1	[W m $^{-1}$ K $^{-1}$]	Thermal conductivity of material 1
k_2	[W m $^{-1}$ K $^{-1}$]	Thermal conductivity of material 2
$k_{contact}$	[W m $^{-1}$ K $^{-1}$]	Harmonic mean of contacting surface conductivities
L	[m]	Vertical length
L_c	[m]	Characteristic length
$m_{asp,1}$	[]	Asperities average slope (surface roughness) of material 1
$m_{asp,2}$	[]	Asperities average slope (surface roughness) of material 2
m_{asp}	[]	Asperities average slope (surface roughness)
Nu	[]	Nusselt number
p	[MPa]	Contact pressure
Pr	[]	Prandtl number
Q_e	[W m $^{-3}$]	Electromagnetic heat source
Q_j	[A m $^{-2}$]	Current source
t	[s]	Time
T_s	[K]	Surface temperature

T_∞	[K]	Ambient temperature
V	[V]	Electric potential

References

- Mathijssen D. Leading the way in thermoplastic composites. *Reinforced Plastics* 2016; 60(6): 405–407. DOI:10.1016/j.repl.2015.08.067. URL <http://dx.doi.org/10.1016/j.repl.2015.08.067>.
- Penumadu D, Murray RE, Cousins D et al. Manufacturing and Flexural Characterization of Infusion-Reacted Thermoplastic Wind Turbine Blade Subcomponents. *Applied Composite Materials* 2019; DOI:10.1007/s10443-019-9760-2.
- Cogswell FN. *Thermoplastic aromatic polymer composites: a study of the structure, processing, and properties of carbon fibre reinforced polyetheretherketone and related materials*. Butterworth-Heinemann, 1992. ISBN 9780750610865.
- Hou M and Friedrich K. Resistance welding of continuous glass fibre-reinforced polypropylene composites. *Compos Manuf* 1992; 3(3): 153–163. DOI:10.1016/0956-7143(92)90078-9.
- Ageorges C, Ye L and Hou M. Advances in fusion bonding techniques for joining thermoplastic matrix composites: A review. *Composites - Part A: Applied Science and Manufacturing* 2001; 32(2001): 839–857. DOI:10.1016/S1359-835X(00)00166-4.
- Stavrov D and Bersee HEN. Resistance welding of thermoplastic composites—an overview. *Composites Part A: Applied Science and Manufacturing* 2005; 36: 39–54. DOI:10.1016/j.compositesa.2004.06.030.
- Dubé M. *Static and fatigue behaviour of thermoplastic composite laminates joined by resistance welding*. Phd thesis, McGill University, 2007.
- Shi H. *Resistance welding of thermoplastic composites: Process and performance*. PhD Thesis, TU Delft, Delft University of Technology, 2014.
- Brassard D, Dubé M and Tavares JR. Resistance welding of thermoplastic composites with a nanocomposite heating element. *Composites Part B: Engineering* 2019; 165: 779–784. DOI:10.1016/j.compositesb.2019.02.038. URL <https://linkinghub.elsevier.com/retrieve/pii/S1359836818322649>.
- Eveno EC and Gillespie JW. Resistance Welding of Graphite Polyetheretherketone Composites: An Experimental Investigation. *Journal of Thermoplastic Composite Materials* 1988; 1(4): 322–338. DOI:10.1177/089270578800100402.
- Brassard D, Dubé M and Tavares JR. Figures and data for the article : "Modelling resistance welding of thermoplastic composites with a nanocomposite heating element", 2020. DOI: 10.5281/zenodo.3988721. URL <https://doi.org/10.5281/zenodo.3988721>.

12. Shi H, Villegas IF and Bersee HEN. Strength and failure modes in resistance welded thermoplastic composite joints: Effect of fibre-matrix adhesion and fibre orientation. *Compos Part A Appl Sci Manuf* 2013; 55: 1–10. DOI:10.1016/j.compositesa.2013.08.008.
13. Dubé M, Hubert P, Yousefpour a et al. Resistance welding of thermoplastic composites skin/stringer joints. *Compos Part A Appl Sci Manuf* 2007; 38: 2541–2552. DOI: 10.1016/j.compositesa.2007.07.014.
14. Dube M, Hubert P, Gallet JN et al. Metal mesh heating element size effect in resistance welding of thermoplastic composites. *J Compos Mater* 2012; 46: 911–919. DOI: 10.1177/0021998311412986.
15. Dubé M, Hubert P, Yousefpour A et al. Fatigue failure characterisation of resistance-welded thermoplastic composites skin/stringer joints. *Int J Fatigue* 2009; 31(4): 719–725. DOI: 10.1016/j.ijfatigue.2008.03.012.
16. Shi H, Villegas IF and Bersee HE. Analysis of void formation in thermoplastic composites during resistance welding. *Journal of Thermoplastic Composite Materials* 2017; 30(12): 1654–1674. DOI:10.1177/0892705716662514. URL <http://journals.sagepub.com/doi/10.1177/0892705716662514>.
17. Ageorges C and Ye L. Simulation of impulse resistance welding for thermoplastic matrix composites. *Applied Composite Materials* 2001; 8(2): 133–147. DOI:10.1023/A:1011229120375.
18. Talbot E, Hubert P, Dube M et al. Optimization of thermoplastic composites resistance welding parameters based on transient heat transfer finite element modeling. *Journal of Thermoplastic Composite Materials* 2013; 26(5): 699–717. DOI:10.1177/0892705711428657.
19. Colak ZS, Sonmez FO and Kalenderoglu V. Process Modeling and Optimization of Resistance Welding for Thermoplastic Composites. *J Compos Mater* 2002; 36(6): 721–744. DOI:10.1177/0021998302036006507. URL <http://journals.sagepub.com/doi/10.1177/0021998302036006507>.
20. Shi H, Villegas IF, Octeau MA et al. Continuous resistance welding of thermoplastic composites: Modelling of heat generation and heat transfer. *Compos Part A Appl Sci Manuf* 2015; 70: 16–26. DOI:10.1016/j.compositesa.2014.12.007.
21. Mijovic J and Wijaya J. Effects of graphite fiber and epoxy matrix physical properties on the temperature profile inside their composite during cure. *SAMPE J; (United States)* 1989; 25.
22. Ageorges C and Ye L. Resistance welding of thermosetting composite/thermoplastic composite joints. *Compos - Part A Appl Sci Manuf* 2001; 32(2001): 1603–1612. DOI:10.1016/S1359-835X(00)00183-4. URL <http://www.sciencedirect.com/science/article/pii/S1359835X00001834>.

23. Incropera FP, DeWitt DP, Bergman TL et al. *Fundamentals of Heat and Mass Transfer, Dekker Mechanical Engineering*, volume 6th. John Wiley & Sons, 2007. ISBN 9780471457282. DOI:10.1016/j.applthermaleng.2011.03.022. URL http://www.osti.gov/energycitations/product.biblio.jsp?osti{_}id=6008324.1105-.
24. Cooper MG, Mikic BB and Yovanovich MM. Thermal contact conductance. *International Journal of Heat and Mass Transfer* 1969; 12(3): 279–300. DOI:10.1016/0017-9310(69)90011-8.
25. Rumble J. *CRC Handbook of Chemistry and Physics, 100th Edition*. CRC Handbook of Chemistry and Physics, CRC Press LLC, 2019. ISBN 9781138367296.
26. Katsounaros A. *Characterization of Multi-Wall Carbon Nanotubes and their Applications*. Phd thesis, Queen Mary, University of London, 2011.
27. Huang YY and Terentjev EM. Dispersion of carbon nanotubes: Mixing, sonication, stabilization, and composite properties. *Polymers (Basel)* 2012; 4(1): 275–295. DOI: 10.3390/polym4010275.
28. Al-Saleh MH and Sundararaj U. A review of vapor grown carbon nanofiber/polymer conductive composites. *Carbon NY* 2009; 47(1): 2–22. DOI:10.1016/j.carbon.2008.09.039.
29. Carroccio S, Puglisi C and Montaudo G. Thermal degradation mechanisms of polyetherimide investigated by direct pyrolysis mass spectrometry. *American Chemical Society, Polymer Preprints, Division of Polymer Chemistry* 2000; 41(1): 684–685.
30. Bastien LJ and Gillespie JW. A non-isothermal healing model for strength and toughness of fusion bonded joints of amorphous thermoplastics. *Polymer Engineering and Science* 1991; 31(24): 1720–1730. DOI:10.1002/pen.760312406.
31. Mu M, Clarke N, Composto RJ et al. Polymer diffusion exhibits a minimum with increasing single-walled carbon nanotube concentration. *Macromolecules* 2009; 42(18): 7091–7097. DOI:10.1021/ma901122s.
32. Kabanemi KK and Hétu JF. A reptation-based model to the dynamics and rheology of linear entangled polymers reinforced with nanoscale rigid particles. *Journal of Non-Newtonian Fluid Mechanics* 2010; 165(15-16): 866–878. DOI:10.1016/j.jnnfm.2010.04.006.

Supplemental material

Tables 5 to 8 present a summary of all the materials properties used in the model.

The relative permittivity for the PEI/MWCNT nanocomposite was calculated with the law of mixture from the reported value of 3.15 for SABIC's PEI grade ULTEM 1010 and a relative permittivity of 15 for MWCNTs²⁶.

Temperature [°C]	CF/PEEK [J kg ⁻¹ K ⁻¹]	PEI/MWCNT [J kg ⁻¹ K ⁻¹]	Alumina Silicate [J kg ⁻¹ K ⁻¹]	Copper [J kg ⁻¹ K ⁻¹]	GPO3 [J kg ⁻¹ K ⁻¹]
Constant				385	1260
40	926	1059			
97			975		
139	1265				
159	1359				
207		1561			
227		1765			
310	1809				
343	2400				
360	1792				
399	1790	1955			
Source	Measured	Measured	Measured	COMSOL	Suppliers

Table 5. List of all specific heat used in the model

Temperature [°C]	CF/PEEK Parallel [W m ⁻¹ K ⁻¹]	CF/PEEK Perpendicular [W m ⁻¹ K ⁻¹]	PEI/MWCNT [W m ⁻¹ K ⁻¹]	Alumina Silicate [W m ⁻¹ K ⁻¹]	Copper [W m ⁻¹ K ⁻¹]	GPO3 [W m ⁻¹ K ⁻¹]
Constant				5.7	400	0.27
20	2.25	0.55	0.41			
40			0.43			
60			0.43			
110			0.46			
150			0.48			
200	3.02	0.73				
Source	Measured	Measured	Measured	Measured	COMSOL	Suppliers

Table 6. List of all thermal conductivity used in the model

Temperature [°C]	CF/PEEK [kg m ⁻³]	PEI/MWCNT [kg m ⁻³]	Alumina Silicate [kg m ⁻³]	Copper [kg m ⁻³]	GPO3 [kg m ⁻³]
Constant		1320	2500	8700	1800
0	1601				
50	1598				
100	1593				
150	1586				
200	1575				
250	1563				
300	1551				
350	1537				
400	1524				
Source	18	Measured	Measured	COMSOL	Suppliers

Table 7. List of all densities used in the model

		PEI/MWCNT	Copper	
Electrical conductivity	[S m ⁻¹]	80	Measured	5.998×10^7
Relative permittivity	[]	4.3	Calculated	1

Table 8. List of electrical properties for the model